Microscopic coupled-channel calculation of proton and alpha inelastic scattering to the 4^+_1 and 4^+_2 states of $^{24}textrm{Mg}$

AUTHOR(S):

Kanada-En'yo, Yoshiko; Ogata, Kazuyuki

CITATION:

Kanada-En'yo, Yoshiko ...[et al]. Microscopic coupled-channel calculation of proton and alpha inelastic scattering to the 4^+_1 and 4^+_2 states of $^{24}textrm{Mg}$. Progress of Theoretical and Experimental Physics 2021, 2021(4): 043D01.

ISSUE DATE:

2021-04

URL:

http://hdl.handle.net/2433/276906

PTEP
Prog. Theor. Exp. Phys. **2021**, 043D01 (16 pages)
DOI: 10.1093/ptep/ptab029

Microscopic coupled-channel calculation of proton and alpha inelastic scattering to the 4^+_1 and 4^+_2 states of ^{24}Mg

Yoshiko Kanada-En'yo[1,*] and Kazuyuki Ogata[2,3,4]

[1]*Department of Physics, Kyoto University, Kyoto 606-8502, Japan*
[2]*Research Center for Nuclear Physics (RCNP), Osaka University, Ibaraki 567-0047, Japan*
[3]*Department of Physics, Osaka City University, Osaka 558-8585, Japan*
[4]*Nambu Yoichiro Institute of Theoretical and Experimental Physics (NITEP), Osaka City University, Osaka 558-8585, Japan*
*E-mail: yenyo@ruby.scphys.kyoto-u.ac.jp

Received December 21, 2020; Revised February 18, 2021; Accepted February 26, 2021; Published March 15, 2021

The triaxial and hexadecapole deformations of the $K^\pi = 0^+$ and $K^\pi = 2^+$ bands of ^{24}Mg have been investigated by the inelastic scatterings of various probes, including electrons, protons, and alpha(α) particles, for a prolonged time. However, it has been challenging to explain the unique properties of the scatterings observed for the 4^+_1 state through reaction calculations. This paper investigates the structure and transition properties of the $K^\pi = 0^+$ and $K^\pi = 2^+$ bands of ^{24}Mg employing the microscopic structure and reaction calculations via inelastic proton and α scattering. In particular, the $E4$ transitions to the 4^+_1 and 4^+_2 states are reexamined. The structure of ^{24}Mg was calculated employing the variation after the parity and total angular momentum projections in the framework of the antisymmetrized molecular dynamics (AMD). The inelastic proton and α reactions were calculated by the microscopic coupled-channel (MCC) approach by folding the Melbourne g-matrix NN interaction with the AMD densities of ^{24}Mg. Reasonable results were obtained on the properties of the structure, including the energy spectra and $E2$ and $E4$ transitions of the $K^\pi = 0^+$ and $K^\pi = 2^+$ bands owing to the enhanced collectivity of triaxial deformation. The MCC+AMD calculation successfully reproduced the angular distributions of the 4^+_1 and 4^+_2 cross sections of proton scattering at incident energies of $E_p = 40$–100 MeV and α scattering at $E_\alpha = 100$–400 MeV. This is the first microscopic calculation to describe the unique properties of the $0^+_1 \to 4^+_1$ transition. In the inelastic scattering to the 4^+_1 state, the dominant two-step process of the $0^+_1 \to 2^+_1 \to 4^+_1$ transitions and the deconstructive interference in the weak one-step process were essential.

Subject Index D20

1. Introduction

The band structure and deformations of ^{24}Mg have been investigated by various experimental probes, including electromagnetic transitions [1–3] and the inelastic scatterings of electrons [4–10], pions [11], nucleons [12–27], ^{3}He [28,29], and α particles [29–33]. In the positive-parity spectra, the $\{0^+_1, 2^+_1, 4^+_1\}$ and $\{2^+_2, 3^+_1, 4^+_2\}$ states have been assigned to the $K^\pi = 0^+$ ground- and $K^\pi = 2^+$ side-bands, respectively. Regarding these positive-parity bands, the properties of the structure, including the energy spectra and $E2$ transitions, are described by the collective rotation of the prolate (β) deformation with the static or vibrational triaxial (γ) deformation. Moreover, the hexadecapole (β_4) deformations of ^{24}Mg have since been discussed.

To investigate the β_4 deformations of ^{24}Mg, various reaction analyses of the inelastic electron, pion, proton, and α scatterings to the 4^+_1 and 4^+_2 states [5,11–13,15,21–26,29,31] and those of the (quasi-)elastic scattering of heavy ions [34,35] have been performed employing collective models. In the analyses of the inelastic scatterings where the phenomenological fittings of the β_2 and β_4 parameters with and without the γ parameters were performed, the weak (or zero) and remarkable β_4 deformations have been attributed to the $K^\pi = 0^+$ and $K^\pi = 2^+$ bands, respectively. Regarding the $4^+_2(K^\pi = 2^+)$ state, which is strongly populated by inelastic scattering, the angular distribution of the cross sections has been described by parameter fitting. However, for the $4^+_1(K^\pi = 0^+)$ state, such reaction calculations with phenomenological collective models have failed to describe the angular distribution of the (p,p') cross sections. Further, microscopic approaches have been applied to calculate the inelastic scattering of protons [14,27] and the inelastic charge form factors [9,36]; however, no microscopic calculation has succeeded in reproducing the property of the $0^+_1 \to 4^+_1$ transition.

In inelastic scattering, the 4^+_1(4.12 MeV) state is weakly produced compared to the 2^+_2(4.24 MeV) state at close energy. Hence, the 4^+_1 cross sections can only be measured with high-quality excitation spectra, which are sufficient to resolve the degenerating 4^+_1 and 2^+_2 states. It has been revealed that the 4^+_1 form factors that were measured by electron scattering displayed a strange shape (q-dependence), which was different from those of the normal $\lambda = 4$ transitions and the observed 4^+_2 form factors [9]. Furthermore, in the inelastic scattering of protons, a similar strange behavior has been observed in the angular distribution of the 4^+_1 cross sections at incident energies of $E_p \leq 65$ MeV, which was challenging to explain utilizing the one-step cross sections of the distorted-wave Born approximation (DWBA). Detailed analyses have been conducted for proton scattering at $E_p = 15$–50 MeV via coupled-channel (CC) calculations based on a collective model [25,26]. They have suggested the dominant two-step contribution in the 4^+_1 cross sections, and also discussed the effects of the weak direct process of $E4; 0^+_1 \to 4^+_1$ transition.

Nevertheless, the agreement of the result with the data was unsatisfactory, and the inelastic scattering of the proton to the 4^+_1 state is still a puzzle. Similarly, in the α scattering at E_α =104–120 MeV, the multi-step effects proved to be effective in the 4^+_1 cross sections [29,31]. These facts indicate that higher-order effects contribute to the inelastic transitions of the 4^+_1 state. Moreover, there is no fundamental description of the obtained parameters even if the CC calculations with a collective model could qualitatively or quantitatively fit the 4^+_1 cross sections by tuning the adjustable parameters in such phenomenological model analyses, and serious model ambiguity may arise in both the structure and reaction parts. Therefore, a microscopic approach is required to reveal the properties of the 4^+_1 state via inelastic scattering.

In our previous study [37], we investigated the proton and α inelastic scattering off ^{24}Mg via the microscopic coupled-channel (MCC) calculation combined with a microscopic structure calculation within the antisymmetrized molecular dynamics (AMD) [38–41]. In the MCC calculations, CC reaction calculations are conducted with the nucleon–nucleus and α–nucleus potentials constructed by folding effective NN interactions with diagonal (ρ) and transition ($\rho^{\rm tr}$) densities of the target nuclei, which are obtained by microscopic structure models. The successful results of the MCC+AMD approach of the proton and α scatterings off various p- and sd-shell nuclei employing the Melbourne g-matrix NN interaction [48], which is an effective NN interaction in a nuclear medium based on a bare NN interaction of the Bonn B potential [49], are presented in our previous reports [42–47]. One of the advantages of utilizing the Melbourne g-matrix NN interaction in the MCC approach [50–54] is that the interaction exhibits energy and density dependencies and there is no adjustable parameter

in the reaction part owing to its fundamental derivation. Therefore, the structure calculation can be easily combined with the reaction calculation of cross sections to examine the validity of the adopted structure inputs by comparing the calculated results with referenced reaction data. Another advantage of this approach is the fact that the combination of the microscopic structure and reaction calculations can be employed to treat the electric transitions and inelastic proton and α scatterings in a unified manner.

In previous AMD results obtained from the ^{24}Mg structure calculation, there were still challenges in precisely reproducing the structure properties; the excitation energies were overshot and the transition strengths were underestimated. These could indicate that the previous method, AMD with variation after parity (VAP) and total-angular-momentum projections, somewhat underestimates the collectivity of the excited states of ^{24}Mg. Moreover, it failed to reproduce the shape of the observed $0^+_1 \to 4^+_1$ charge form factors, which was a crucial shortcoming in the previous MCC+AMD calculation for the reproduction of the 4^+_1 cross sections of proton and α scattering. In principle, these limitations in ^{24}Mg structure calculation could be improved by the inclusion of higher-order correlations that are beyond the AMD model space with a Slater determinant. However, such an extension of the model space will require huge computational cost. Hence, an alternative treatment in the AMD+VAP framework is employed to overcome this undershooting of the collectivity in this paper. Namely, we apply a version of the AMD+VAP model with fixed nucleon spins instead of optimizing the nucleon spins in the previous version. The fixed-spin version could suitably avoid the undershooting problem of the AMD+VAP model and obtain good results for the collectivity in the *sd*-shell nuclei, as discussed in the structure studies of the shape coexistence phenomena of the nuclei around ^{28}Si [55,56], and has been applied to the MCC+AMD calculations of the $p+^{28}$ Si and $\alpha+^{28}$ Si reactions [45].

Here, we reexamine the transition properties of the positive-parity states of the $K^\pi = 0^+$ and $K^\pi = 2^+$ bands of ^{24}Mg via proton and α inelastic scattering by the MCC+AMD approach, employing improved structure inputs that are obtained by the fixed-spin version of AMD+VAP. Further, we discuss the properties of the 4^+_1 and 4^+_2 states by comparing the calculated cross sections with the experimental data, including the recently observed (α,α') data at $E_\alpha = 130$ and 386 MeV [33].

The paper is organized as follows. Section 2 briefly explains the AMD framework of ^{24}Mg and the MCC approaches for $p + {}^{24}$Mg and $\alpha + {}^{24}$Mg scatterings. The AMD results of the structure properties of ^{24}Mg are described in Sect. 3. Next, Sect. 4 presents the AMD+MCC results of proton and α scattering, and discusses the transition properties of the 4^+ states. Finally, a summary of the study is presented in Sect. 5.

2. Method

In the AMD framework, an A-nucleon wave function is represented by a Slater determinant of single-nucleon Gaussian wave functions as follows:

$$\Phi_{\rm AMD}(\boldsymbol{Z}) = \frac{1}{\sqrt{A!}}\mathcal{A}\{\varphi_1,\varphi_2,\ldots,\varphi_A\}, \tag{1}$$

$$\varphi_i = \phi_{\boldsymbol{X}_i}\chi_i\tau_i, \tag{2}$$

$$\phi_{\boldsymbol{X}_i}(\boldsymbol{r}_j) = \left(\frac{2\nu}{\pi}\right)^{3/4}\exp\left[-\nu(\boldsymbol{r}_j-\boldsymbol{X}_i)^2\right]. \tag{3}$$

In the equations, $\mathcal{A}$ is the antisymmetrizer and φ_i is the ith single-particle wave function written by the product of the spatial ($\phi_{\boldsymbol{X}_i}$), spin (χ_i), and isospin (τ_i) wave functions. The nucleon isospin function,

τ_i, is fixed to be proton or neutron. In the present version of AMD, we fix the nucleon spin function, χ_i, to be an up spin ($\chi_\uparrow$) or down spin ($\chi_\downarrow$). The Gaussian centroid parameters, $\boldsymbol{Z} \equiv \{\boldsymbol{X}_1, \ldots, \boldsymbol{X}_A\}$, of the single-particle wave functions are assumed to be independent complex parameters, which are determined by the energy optimization for each J^π state of ^{24}Mg.

The energy variation is performed after the parity and total angular momentum projections to minimize the energy expectation value, $E = \langle\Psi|\hat{H}|\Psi\rangle/\langle\Psi|\Psi\rangle$, for $\Psi = P^{J\pi}_{MM'}\Phi_{\rm AMD}(\boldsymbol{Z})$ that is projected from the AMD wave function. Here, $P^{J\pi}_{MM'}$ is the parity and total angular momentum projection operator, and M' is the quanta of the Z component (J_Z) of the total angular momentum in the body-fixed frame. Note that M' is not necessarily equal to the K quanta, which is defined by the principal axis of the intrinsic shape, because the principal axis could tilt from the Z-axis during the energy variation. VAP is performed for $J^\pi = 0^+$, 2^+, 3^+, and 4^+ to obtain the states of the $K^\pi = 0^+$ and $K^\pi = 2^+$ bands. We select $M' = 0$, 1, 2, and 2 for $J^\pi = 0^+$, 2^+, 3^+, and 4^+, respectively, so as to obtain the minimum energy $E = \langle\Psi|\hat{H}|\Psi\rangle/\langle\Psi|\Psi\rangle$ after the variation for a given J^π. After VAPs of four sets of J^π and M', the resulting four configurations, $\Phi_{\rm AMD}(\boldsymbol{Z}^{(m)})$ ($m = 1, \ldots, 4$), are superposed to calculate the final wave functions of positive-parity states. Specifically, the diagonalization of the Hamiltonian and norm matrices is performed by the basis wave functions, $P^{J\pi}_{MM'}\Phi_{\rm AMD}(\boldsymbol{Z}^{(m)})$, regarding M' and m, which correspond to the K mixing and configuration mixing, respectively.

In the previous AMD+VAP calculation of ^{24}Mg, the nucleon spin functions, χ_i, were not fixed; they were optimized by the energy variation. In this paper, we name the present and previous AMD+VAP calculations, i.e. those without and with nucleon spin optimization, "AMD(fix-s)" and "AMD(opt-s)," respectively.

The effective nuclear interactions employed in the present structure calculation of AMD(fix-s) are the same as those used in Refs. [37,40,45,46]. The MV1 (Case 1) central force [57] with the parameters $(b, h, m) = (0, 0, 0.62)$, and the spin–orbit term of the G3RS force [58,59] with strength parameters $u_{ls} \equiv u_I = -u_{II} = 3000$ MeV are employed. Coulomb force is also included.

The elastic and inelastic cross sections of the proton and α-particle scatterings off ^{24}Mg are calculated by MCC+AMD in the same way as done in the previous work [37]. The nucleon–nucleus potentials are constructed in a microscopic folding model (MFM) where the diagonal and coupling potentials are calculated by folding the Melbourne g-matrix NN interaction [48] with diagonal ($\rho(r)$) and transition ($\rho^{\rm tr}(r)$) densities of the target nucleus. The α–nucleus potentials are obtained by an extended nucleon–nucleus folding (NAF) model [52], which is obtained by folding the calculated nucleon–nucleus potentials with an α density. For more details of the reaction calculations, the reader is referred to Refs. [37,42–44] and references therein.

For use in the MFM calculation of the nucleon–nucleus potentials, $\rho(r)$ and $\rho^{\rm tr}(r)$ of ^{24}Mg are calculated from the wave functions obtained from AMD(fix-s). The charge symmetry breaking in the wave functions obtained for the $K^\pi = 0^+$ and $K^\pi = 2^+$ bands of ^{24}Mg is less than several percentage points, and hence is omitted in the MFM calculation. Namely, half of the matter densities $\rho(r)/2$ and matter transition densities $\rho^{\rm tr}(r)/2$ are used for the proton and neutron components of the densities in the MFM calculation, where $\rho(r) = (\rho_p(r) + \rho_n(r))$ and $\rho^{\rm tr}(r) = (\rho^{\rm tr}_p(r) + \rho^{\rm tr}_n(r))$, because $\rho_p(r) \approx \rho_n(r)$ and $\rho^{\rm tr}_p(r) \approx \rho^{\rm tr}_n(r)$ are satisfied. The $E2$ and $E4$ transition strengths are calculated by the proton transition densities as

$$B(E\lambda; J_i \to J_f) = \frac{e^2}{2J_f + 1}\left|\int r^\lambda \rho^{\rm tr}_p(r) r^2 dr\right|^2. \tag{4}$$

Table 1. Intrinsic deformations, β and γ (degree), of the $0_1^+(K=0)$, $2_1^+(K=0)$, $4_1^+(K=0)$, and $3_1^+(K=0)$ states of ^{24}Mg obtained by VAP. The deformation parameters are calculated for the intrinsic wave functions of single configurations before the projections and configuration mixing. The AMD(fix-s) result is compared to the AMD(opt-s) one.

J_i^π (band)	AMD(fix-s)	AMD(opt-s)
$0_1^+(K=0)$	$(0.35, 10)$	$(0.35, 3)$
$2_1^+(K=0)$	$(0.37, 12)$	$(0.33, 6)$
$4_1^+(K=0)$	$(0.37, 12)$	$(0.29, 7)$
$3_1^+(K=2)$	$(0.37, 20)$	$(0.34, 12)$

Similarly, the isoscalar transition strengths are given as

$$B(\mathrm{IS}\lambda; J_i \to J_f) = \frac{e^2}{2J_f+1}\left|\int r^\lambda \rho^{\mathrm{tr}}(r) r^2 dr\right|^2 \approx 4B(E\lambda; J_i \to J_f). \tag{5}$$

To reduce the model ambiguity of the structure calculation, the calculated $\rho^{\mathrm{tr}}(r)$ are renormalized by the factor f^{tr} as $\rho^{\mathrm{tr}}(r) \to f^{\mathrm{tr}}\rho^{\mathrm{tr}}(r)$ to fit the experimental electromagnetic transition strengths and charge form factors. For the excitation energies of ^{24}Mg, the experimental values are utilized.

3. Structure of ^{24}Mg

In this section we present the AMD(fix-s) results of the structure calculation of ^{24}Mg and compare them to the previous AMD(opt-s) results.

First, we analyze each AMD configuration, which are obtained by VAP for the $0_1^+(K=0)$, $2_1^+(K=0)$, $4_1^+(K=0)$, and $3_1^+(K=2)$ states, before the superposition to discuss the intrinsic shapes of these states. Table 1 presents the deformation parameters, β and γ, obtained from the expectation values, $\langle X^2\rangle$, $\langle Y^2\rangle$, and $\langle Z^2\rangle$, of the intrinsic wave functions without the parity and total angular momentum projections. The result of the AMD(fix-s) calculation is compared to that of the AMD(opt-s) calculation. The AMD(fix-s) calculation obtains larger γ values than the previous calculation, implying that the triaxial collectivity is enhanced in the AMD(fix-s) result, in which the β and γ values are almost constant in the $K^\pi = 0^+$ ground-band.

The intrinsic density distribution of the AMD(fix-s) result is displayed in Fig. 1. From the density distribution, the intrinsic states exhibit higher-order correlations beyond the quadrupole deformations, including the cluster components. Moreover, the intrinsic structure change occurs with an increase in J along the $K^\pi = 0^+$ ground-band even though the quadrupole deformations are almost unchanged.

Next, we discuss the structure properties obtained by the K mixing and configuration mixing after the parity and total angular momentum projections. Figure 2 shows a comparison between the AMD(fix-s) and AMD(opt-s) results of the energy spectra with the experimental data of the ground-band ($K^\pi = 0^+$) and side-band ($K^\pi = 2^+$). In the calculations, the $K^\pi = 2^+$ band, including the 2_2^+, 3_1^+, and 4_2^+ states, is constructed by the triaxially deformed intrinsic shape and regarded as the side-band of the $K^\pi = 0^+$ ground-band. Because of the enhanced triaxiality, the overshooting shortcoming of the calculated $K^\pi = 2^+$ band energy, which was observed in the AMD(opt-s) result, is sufficiently improved, and a good correlation with the data is obtained in the AMD(fix-s) result.

The AMD(fix-s) and AMD(opt-s) results of the $E2$ transition strengths, $B_{\mathrm{th}}(E2)$, are listed in Table 2 and compared to the experimental data, ($B_{\mathrm{exp}}(E2)$). The previous AMD(opt-s) calculation

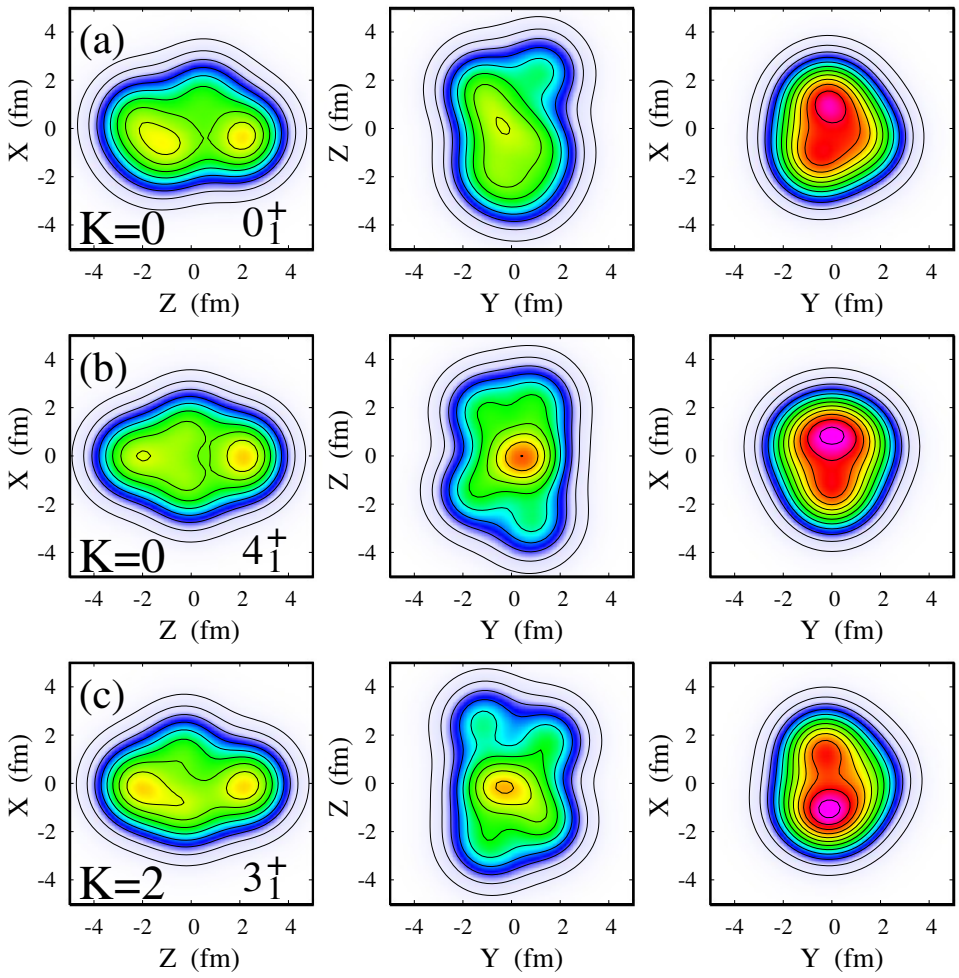

Fig. 1. Density distribution of the intrinsic wave functions before the parity and total angular momentum projections of the $0^+_1(K^\pi = 0^+)$, $4^+_1(K^\pi = 0^+)$, and $3^+_1(K^\pi = 2^+)$ states obtained by VAP. In the left, middle, and right panels, the densities are projected onto the X–Z, Y–Z, and Y–X planes by integrating along the Y, X, and Z axes, respectively. The intrinsic axes are selected as the principal axes in the following order: $\langle ZZ\rangle \geq \langle YY\rangle \geq \langle XX\rangle$.

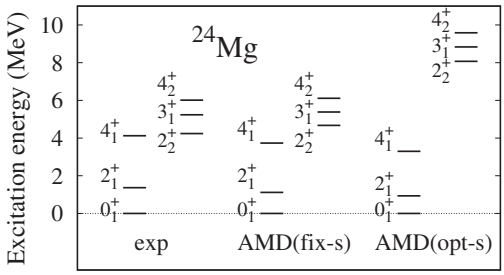

Fig. 2. Energy spectra of ^{24}Mg for the $K^\pi = 0^+$ ground-band and $K^\pi = 2^+$ side-band. The calculated spectra of the AMD(fix-s) and AMD(opt-s) results are compared to the experimental spectra [60].

underestimated the in-band $E2$ transition strengths by a factor of two, but the results are enhanced in the AMD(fix-s) calculation. A possible reason for these improvements in the energy spectra and

Table 2. $E2$ transition strengths and the electric Q moment of ^{24}Mg. The experimental data are from Refs. [1, 3,60]. The $B_{\rm th}$ values obtained by AMD(fix-s) are listed with the renormalization factors, $f^{\rm tr}$, employed for the reaction calculations. For comparison, the values of AMD(opt-s) from Ref. [37] are also listed. The units of the $E2$ transition strengths and Q moments are e^2 fm^4 and e fm^2, respectively.

		exp [60]	exp [1]	exp [3]	AMD(opt-s) [37]		AMD(fix-s)		
J_i^π	J_f^π	$B(E2)$	$B(E2)$	$B(E2)$	$B_{\rm th}(E2)$	$f^{\rm tr}$	$B_{\rm th}(E2)$	$f^{\rm tr}$ set-I	$f^{\rm tr}$ set-II
2_1^+	0_1^+	88.4(4.1)	84.3(2.5)	86.5(1.6)	55.4	1.26	70.2	1.12	1.12
4_1^+	2_1^+	160(16)	95(16)	155(12)	72.8	1.48	101.7	1.26	1.11[a]
3_1^+	2_2^+	240(30)	140(25)	157(23)	103.1		120.3		
4_2^+	2_2^+	77(10)	66(12)	76.9(9.9)	36.2	1.46	41.2	1.37	1.37
4_2^+	3_1^+				73.3		81.7		
2_2^+	0_1^+	8.0(0.8)	5.8(1.2)	6.5(0.5)	2.1	1.95	3.2	1.58	1.58
2_2^+	2_1^+	12.2(0.9)	11.1(1.6)	12.2(0.9)	0.6	1[b]	4.1	1.72	1.72
3_1^+	2_1^+	10.3(1.2)	8.6(1.2)	9.6(0.9)	3.1		5.6		
4_2^+	2_1^+	4.1(0.4)		4.1(0.4)	2.9	1.19	0.1	1[b]	1[b]
		exp [60]							
J^π		Q			Q		Q		
2_1^+		−16.6(6)			−15.1		−17.0		

[a]Fitting the mean value of Refs. [1,3]. [b]No renormalization.

transition strengths of the AMD(fix-s) calculation is the following: in the one-Slater description of the AMD+VAP framework, the optimization of the nucleon spins possibly smears the collectivity of the deformations in the med-*sd*-shell nuclei, but the smearing effect is weakened by fixing the nucleon spins in the AMD(fix-s) calculation. Nevertheless, to precisely fit the data of the in-band transition strengths, a 10%–40% enhancement of the transition matrix elements is still required of the AMD(fix-s) result.

For use in the MCC calculation, we renormalize the calculated $\rho^{\rm tr}(r)$ with the factors $f^{\rm tr} = \sqrt{B_{\rm exp}(E2)/B_{\rm th}(E2)}$ to reproduce the experimental transition strengths. In the default MCC calculation, we utilize the $f^{\rm tr}$ values that are adjusted $B_{\rm exp}(E2)$ values from Ref. [60] in which the evaluation was performed with a couple of data sets of lifetime measurements. We call this choice "$f^{\rm tr}$(set-I)." In Table 2, we also present two data sets reported in Refs. [1,3]. For most of the transitions, the two measurements obtained consistent $B(E2)$ values, but inconsistent values for the $4_1^+ \to 2_1^+$ transition. To discuss the effect of this ambiguity on the reaction analysis, we adopt another choice of renormalization $f^{\rm tr}$ for the $4_1^+ \to 2_1^+$ transition by fitting the mean value of the two data. We call this optional choice "$f^{\rm tr}$(set-II)." The adopted $f^{\rm tr}$ values of the default case (set-I) and the optional case (set-II) are listed in Table 2. The only difference between $f^{\rm tr}$(set-I) and $f^{\rm tr}$(set-II) is the value for the $4_1^+ \to 2_1^+$ transition.

The $E2$ and $E4$ transition strengths of the inelastic transitions from the ground state are listed in Table 3, where the calculated values of the isoscalar (IS) components, $B(\mathrm{IS}\lambda)/4$, are listed together with the experimental values, $B(E\lambda)$, measured by γ decays, and the empirical values, $B(C\lambda)$, which were evaluated by the (e,e') and (π,π') data, and $B(\mathrm{IS}\lambda)/4$ by the (α,α') data. The $E4$ transition strengths from the ground state concentrate in the 4_2^+ state, whereas the transition to the 4_1^+ state is much weaker. Compared to the AMD(opt-s) result, a significant improvement is achieved for the $4_1^+ \to 0_1^+$ transition employing the AMD(fix-s) calculation, which yields an $E4$ transition strength

Table 3. $E2$ and $E4$ transition strengths of the $2^+ \to 0_1^+$ and $4^+ \to 0_1^+$ transitions. For the experimental values, $B(E\lambda)$ from the γ decay data [60], $B(C\lambda)$ from the (e,e') data [7,9], $B(\mathrm{IS}\lambda)/4$ from the (α,α') data [32], and $B(C\lambda)$ from the (π,π') data [11] are listed. Regarding the theoretical values of the present AMD(fix-s) calculation, the original values $B_{\mathrm{th}}(\mathrm{IS}\lambda)/4$ before the renormalization and the renormalized values $f_{\mathrm{tr}}^2 B_{\mathrm{th}}(\mathrm{IS}\lambda)/4$ are listed together with the renormalization factors f^{tr}(set-I, set-II), which are common for the set I and II cases. The unit of the transition strengths is $e^2\,\mathrm{fm}^{2\lambda}$. For comparison, the AMD(opt-s) results of the original $B_{\mathrm{th}}(\mathrm{IS}\lambda)/4$ values before the renormalization and the f^{tr} values from Ref. [37] are also listed.

J^π (band)	γ decays [60] $B(E\lambda\downarrow)$	(e,e') [9] $B(C\lambda\downarrow)$	(e,e') [7] $B(C\lambda\downarrow)$	(α,α') [32] $B(\mathrm{IS}\lambda\downarrow)/4$	(π,π') [11] $B(C\lambda\downarrow)$
2_1^+ $(K=0)$	88.4(4.1)	90.6(7.0)	105(5)	84	108
2_2^+ $(K=2)$	8.0(0.8)	5.48(0.60)	5.26(1.2)	14	6.7
4_1^+ $(K=0)$		200(30)		1200	
4_2^+ $(K=2)$		4800(600)	4700(1100)	4700	2900

J^π (band)	AMD(opt-s)		AMD(fix-s)		
	$B(\mathrm{IS}\lambda\downarrow)/4$	f^{tr}	$B(\mathrm{IS}\lambda\downarrow)/4$		f^{tr}
	original		original	normalized	
2_1^+ $(K=0)$	54	1.26	68	86	1.12[b]
2_2^+ $(K=2)$	2.0	1.95	3.1	7.7	1.58[b]
4_1^+ $(K=0)$	1.1	1[a]	243	477	1.4[c]
4_2^+ $(K=2)$	1740	1.66	3350	4050	1.1[c]

[a]No renormalization. [b]f^{tr} determined to fit the $B(E\lambda)$ data [60]. [c]f^{tr} determined to fit the charge form factors [9].

comparable to the empirical value of the (e,e') data. Notably, the evaluation of $B(IS)/4$ by the (α,α') data was inconsistent with the value $B(C4)$ of the (e,e') data, because the DWBA calculation was performed in the reaction analysis of 120 MeV α scattering data in Ref. [32], although it was not applicable to the 4_1^+ cross sections, as will be discussed subsequently.

Regarding the $E4$ transitions, we determine f^{tr} by fitting the inelastic charge form factors to the 4_1^+ and 4_2^+ states measured by electron scattering. The adopted f^{tr} values and the transition strengths after the renormalization are listed in Table 3. The values are $f^{\mathrm{tr}} = 1.4$ and 1.1 for the 4_1^+ and 4_2^+ states, respectively, implying that 40% and 10% enhancements are still required to fit the observed charge form factors.

The squared elastic and inelastic charge form factors are shown in Fig. 3, which shows a comparison between the renormalized inelastic form factors and the data measured by electron scattering. The AMD(fix-s) calculation successfully describes the shapes of the experimental form factors, and precisely reproduces the shapes and magnitude of the observed form factors after the renormalization. The significant state dependence of the $E4$ transitions can be observed between the 4_1^+ and 4_2^+ states in both the magnitude and shape of the form factors. In the form factors in the range of the transfer momentum, $q \leq 3\ \mathrm{fm}^{-1}$, the 4_1^+ state exhibits a narrow two-peak structure that is different from the broader shape of the 4_2^+ form factors. This result is the first microscopic calculation that successfully describes this unique character of the shape of the 4_1^+ form factors, which had been a challenge to reproduce by structure calculations.

The calculated matter $\rho(r)$ and the renormalized $\rho^{\mathrm{tr}}(r)$ of the AMD(fix-s) result are shown in Fig. 4. The unusual behavior of the $0_1^+ \to 4_1^+$ transition density that corresponds to the two-peak structure of the charge form factors can be observed. For comparison, the Fermi density,

$$\rho_{\mathrm{Fermi}}(r) = \frac{\rho_0}{1+\exp\left(\frac{r-c}{t/4.4}\right)}, \tag{6}$$

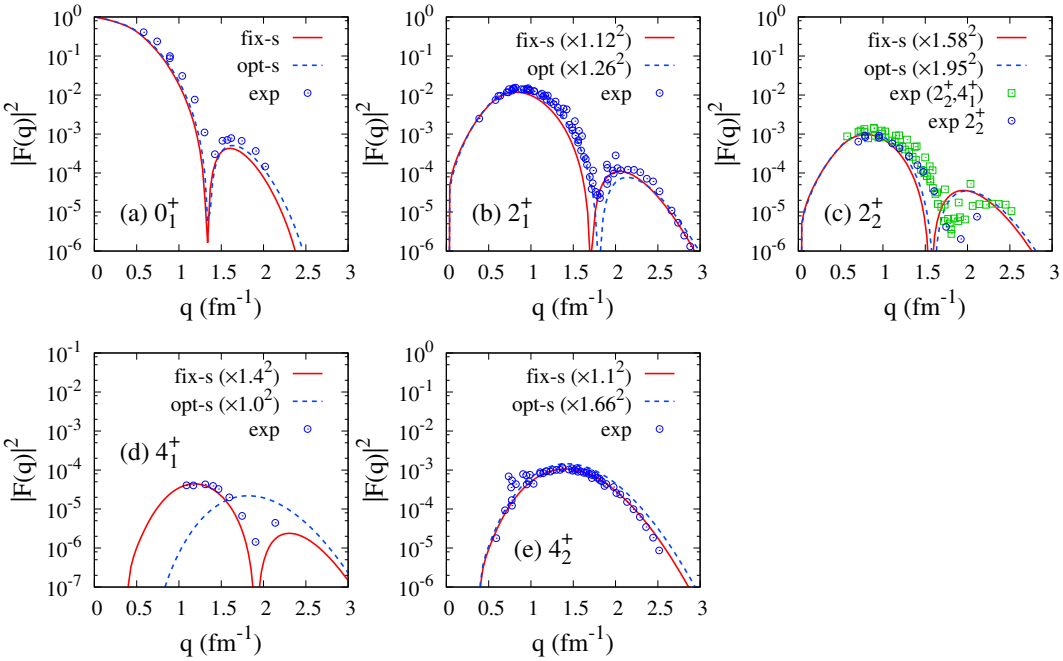

Fig. 3. Squared charge form factors of the elastic and inelastic processes of ^{24}Mg. For the AMD(fix-s) result, the renormalized form factors multiplied by the $f^{\rm tr}$ values in Table 3 are plotted. For comparison, the AMD(opt-s) result of the renormalized form factors are also shown. The experimental data are those measured by electron scattering [4,6–9]. In the data for the 2_2^+(4.24 MeV) state in Refs. [4,6,8], the 4_1^+(4.12 MeV) contribution was not separated.

with $c = 2.876$ fm and $t = 2.333$ fm, and the collective-model transition density of the Fermi-type Tassie form, $\rho^{\rm tr}_{\rm Tassie}(r) \propto r^{\lambda-1}\partial\rho_{\rm Fermi}(r)/\partial r$, are shown in the figure. $\rho^{\rm tr}(r)$ of $0_1^+ \to 4_2^+$ has the dominant peak at the nuclear surface, consistent with the standard $E4$ transition as shown by the collective-model $\rho^{\rm tr}(r)$. Conversely, the behavior of $\rho^{\rm tr}(r)$ of $0_1^+ \to 4_1^+$ is very different from that for the standard $E4$ transition: it exhibits an enhanced amplitude in the outer region and some suppression in the inner region. In the AMD(fix-s) result, this dominant amplitude in the outer region is produced by dynamical effects beyond the static mean field, and its origin is determined by deconstructive contributions from various types of excitations, including the α-cluster dynamics at the nuclear surface and the ^{16}O-core excitation.

For comaprison, the renormalized form factors and transition densities of the previous AMD(opt-s) calculation are also shown in Figs. 3 and 4, respectively. After the renormalization, the previous AMD(opt-s) results are consistent with the present AMD(fix-s) results except for the $0_1^+ \to 4_1^+$ transition, for which the AMD(opt-s) calculation gives quite different form factors from the AMD(fix-s) ones and fails to describe the experimental data.

4. Proton and α scattering

MCC+AMD calculations are performed for the proton and α scattering employing the diagonal and transition densities obtained by AMD(fix-s). The $J^\pi = 0_1^+, 2_1^+, 2_2^+, 4_1^+$, and 4_2^+ states of ^{24}Mg and $\lambda = 0$, 2, and 4 transitions between them are included in the CC calculations, which we call the full CC calculations. In the default MCC+AMD calculations, the calculated transition densities are renormalized by the factors $f^{\rm tr}$(set-I), which are listed in Tables 2 and 3. We calculate the elastic and

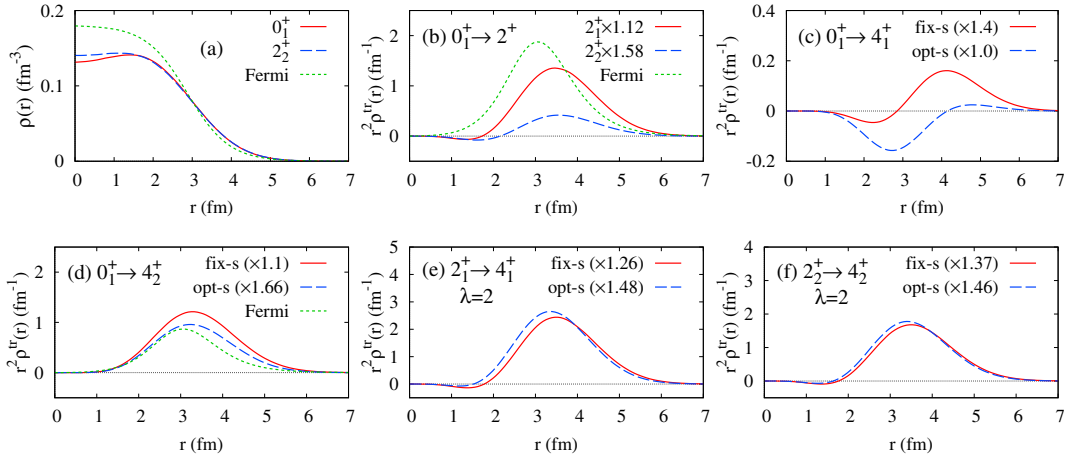

Fig. 4. Calculated matter densities $\rho(r)$ and transition densities $\rho^{\rm tr}(r)$ of ^{24}Mg obtained by the present AMD(fix-s) calculation. The renormalized transition densities, $f^{\rm tr}\rho^{\rm tr}_{\rm th}$, employing the factors $f^{\rm tr}$ listed in Table 3, are shown. For comparison, the Fermi density $\rho_{\rm Fermi}(r) = \rho_0[1+\exp(\frac{r-c}{t/4.4})]^{-1}$ with $c = 2.876$ fm and $t = 2.333$ fm, and the collective-model transition densities of the Fermi-type Tassie form, $\rho^{\rm tr}_{\rm Tassie}(r) \propto r^{\lambda-1}\partial\rho_{\rm Fermi}(r)/\partial r$, are shown. $\rho^{\rm tr}_{\rm Tassie}(r)$ is normalized to fit the $B(E2; 2^+_1 \to 0^+_1)$ and $B(E4; 4^+_2 \to 0^+_1)$ of the AMD(fix-s) result. The previous AMD(opt-s) results from Ref. [37] are also shown in panels (c)–(f).

inelastic cross sections of the proton scattering at incident energies of $E_p = 40$, 49, 65, and 100 MeV, and α scattering at $E_\alpha = 104$, 120, 130, and 386 MeV. To observe the CC effects, the one-step cross sections are also calculated by DWBA, employing the same inputs. It should be commented that the procedures for the reaction calculations in this paper are, in principle, the same as those in Ref. [37] except for the structure inputs; the revised diagonal and transition densities of ^{24}Mg obtained by AMD(fix-s) are utilized in the present calculation instead of the AMD(opt-s) densities in the previous calculation.

The calculated proton scattering cross sections are shown in Fig. 5 and compared to the experimental data. The present MCC+AMD calculation reasonably reproduces the amplitudes of the elastic and inelastic cross sections of proton scattering within this energy range. It also reproduces the diffraction patterns around the peak positions. The dip structures of the elastic cross section data cannot be reproduced by the present MCC+AMD calculation, which is mainly due to the absence of the spin–orbit potentials. The dashed lines represent the elastic cross sections obtained with the one-channel calculation including the microscopic central potential together with a phenomenological spin–orbit potential [61]. Although a slight disagreement around the dips remains, the inclusion of the phenomenological spin–orbit potential improves the agreement with the elastic scattering data significantly. This has been pointed out in previous studies [50,63]. In Ref. [63], in a phenomenological approach, it was shown that the spin–orbit potential hardly affects the inelastic cross sections. According to this finding, it is expected that the present results for the proton inelastic cross sections shown in Fig. 5 will not change if a spin–orbit potential is implemented in the MCC calculation. Compared to the DWBA calculation, it is observed that the one-step process contributes dominantly to the proton scattering cross sections except in the 4^+_1 state. For the proton inelastic scattering to the 4^+_1 state, the MCC+AMD calculation reproduces the amplitude and angular distribution around the first and second peaks, whereas the DWBA cross sections are inconsistent in both amplitude and angular distribution. The successful result for the 4^+_1 cross sections, which could not be obtained by

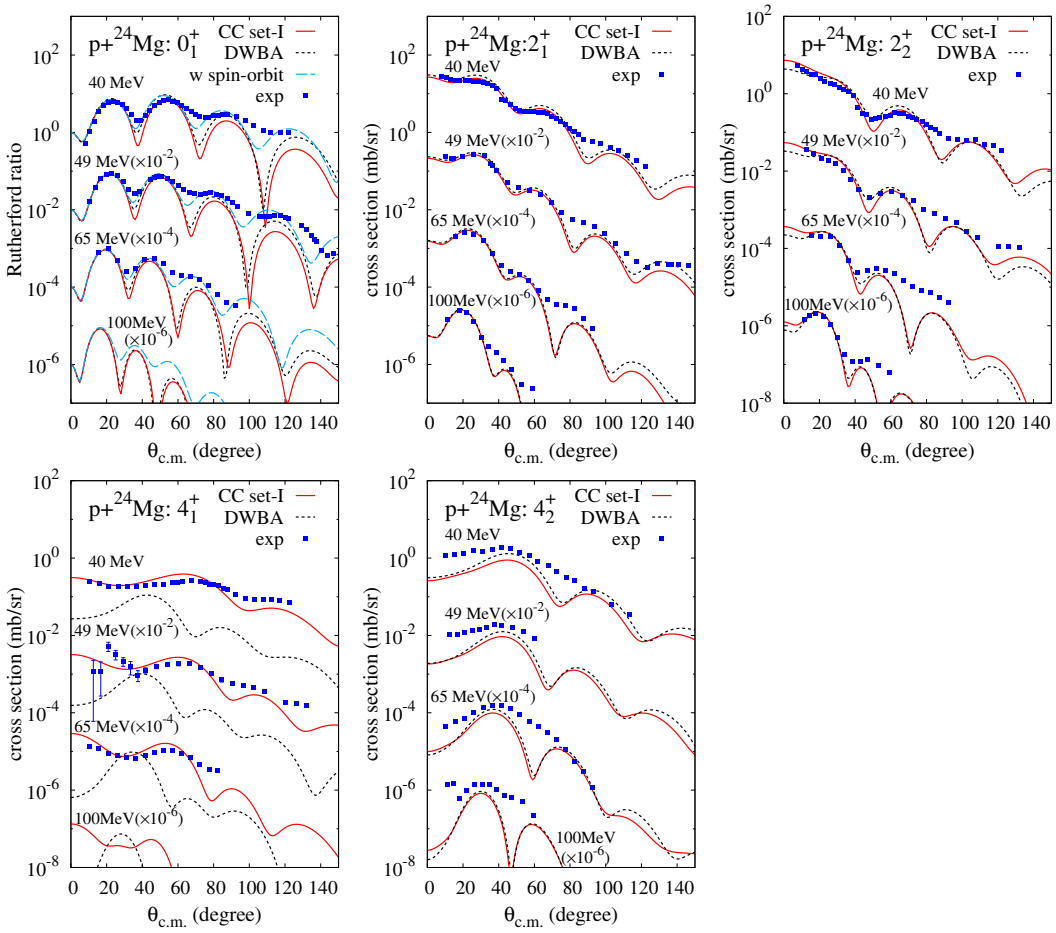

Fig. 5. Cross sections of the elastic and inelastic proton scattering off ^{24}Mg at $E_p = 40$, 49, 65, and 100 MeV calculated by MCC+AMD (solid lines with label "CC set-I") and DWBA (dotted lines) employing $f^{\rm tr}$(set-I). The elastic cross sections obtained with the one-channel calculation by including the microscopic central potential together with a phenomenological spin–orbit potential [61] are also shown (dashed lines with label "w spin-orbit." The experimental data are the cross sections at $E_p = 40$ [13,14], 49 [17], 65 [19,62], and 100 MeV [20,62].

the AMD(opt-s) densities in the previous MCC+AMD calculation, is a new result of the the present MCC+AMD calculation by employing the AMD(fix-s) densities.

The results of the α scattering are shown in Fig. 6. The calculated elastic and inelastic cross sections are compared to the experimental data. The MCC+AMD calculation adequately reproduces the amplitudes and angular distributions of the existing data at an energy range of $E_\alpha = 100$–400 MeV. The good agreements with the experimental cross sections for the 0^+_1, 2^+_1, 2^+_2, and 4^+_2 states are obtained by the present MCC+AMD calculation employing the AMD(fix-s) densities consistently with the previous results obtained with the AMD(opt-s) densities. The present calculation also succeeds in reproducing the 4^+_1 cross sections, for which the AMD(opt-s) densities in the previous MCC+AMD calculation failed to describe the experimental data. Compared to the one-step cross sections of DWBA, significant CC effects are observed in the 4^+_1 and 4^+_2 cross sections. In particular, the one-step cross sections of the 4^+_1 state are inconsistent with the amplitude and angular distribution of the observed (α, α') data, thereby implying that the multi-step process is also essential for the α inelastic scattering to the 4^+_1 state.

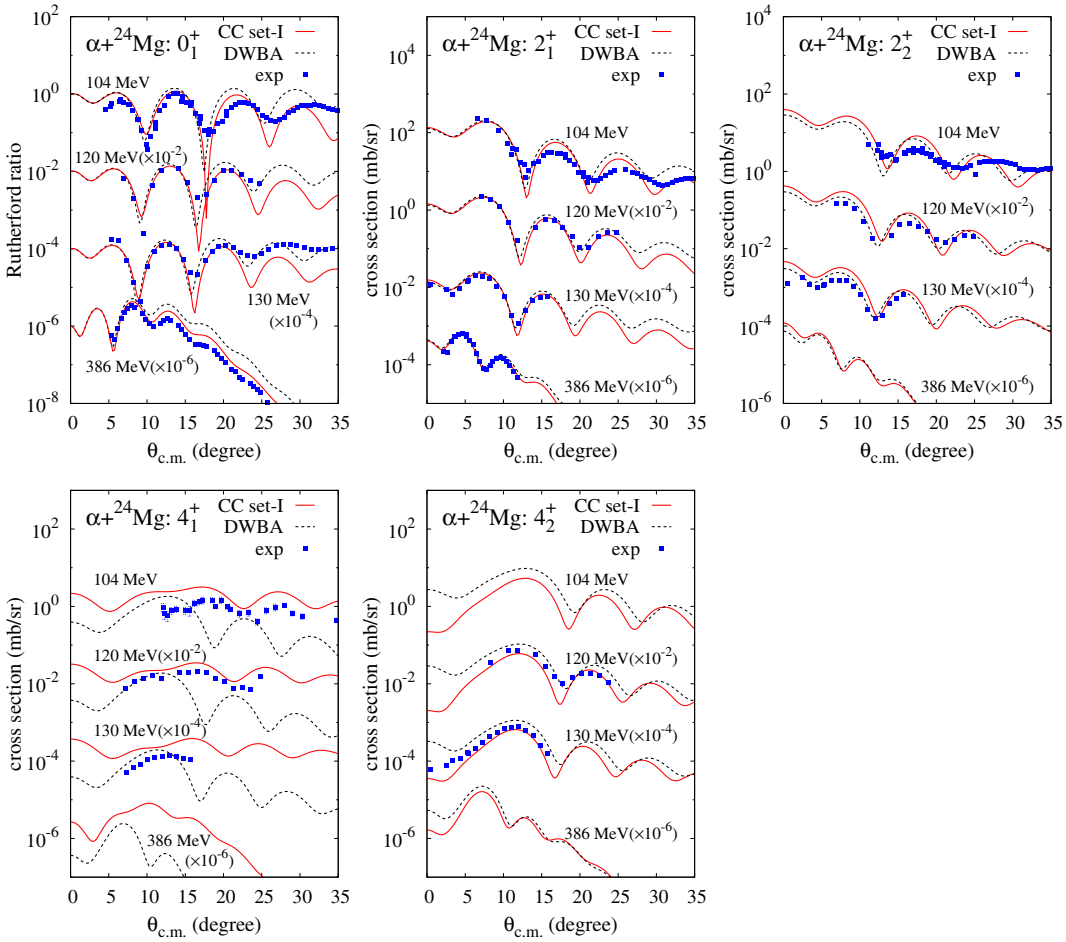

Fig. 6. Cross sections of elastic and inelastic α scattering off ^{24}Mg at $E_\alpha = 104$, 120, 130, and 386 MeV calculated by MCC+AMD (solid lines with label "CC set-I") and DWBA (dotted lines) employing $f^{\rm tr}$(set-I). The experimental data are the cross sections at $E_\alpha = 104$ [31,62], 120 [32], 130 [33], and 386 MeV [33].

To acquire more details on the direct and multi-step contributions to the 4^+_1 cross sections of proton and α scatterings, we conduct the CC calculations by omitting the $0^+_1 \to 4^+_1$ transition. We compare the results to the full CC result including all the $\lambda = 0, 2, 4$ transitions. Figure 7 displays the results with and without the $0^+_1 \to 4^+_1$ transition for the 4^+_1 cross sections of proton and α scatterings together with the one-step cross sections of DWBA. In the CC results without the $0^+_1 \to 4^+_1$ transition, the two-step process via the $E2; 0^+_1 \to 2^+_1$ and $E2; 2^+_1 \to 4^+_1$ transitions delivers the dominant contribution to the 4^+_1 cross sections of proton and α scattering. Compared to the two-step contribution, the one-step contribution is more than one order weaker. However, in the full CC results, the direct $0^+_1 \to 4^+_1$ process suppresses the dominant two-step contribution, particularly in the α scattering cross sections, and significantly alters the angular distribution of the 4^+_1 cross sections. This deconstructive interference of the dominant two-step contribution by the one-step process is essential in describing the observed diffraction patterns.

Notably, in the energy systematics, the observed 49 MeV (p, p') data at the forward angles were inconsistent with the data at $E_p = 40$ and 65 MeV in the other experiments. Additionally, in the α scattering data, the 130 MeV (α, α') data were inconsistent with the data at $E_\alpha = 104$ and 120 MeV.

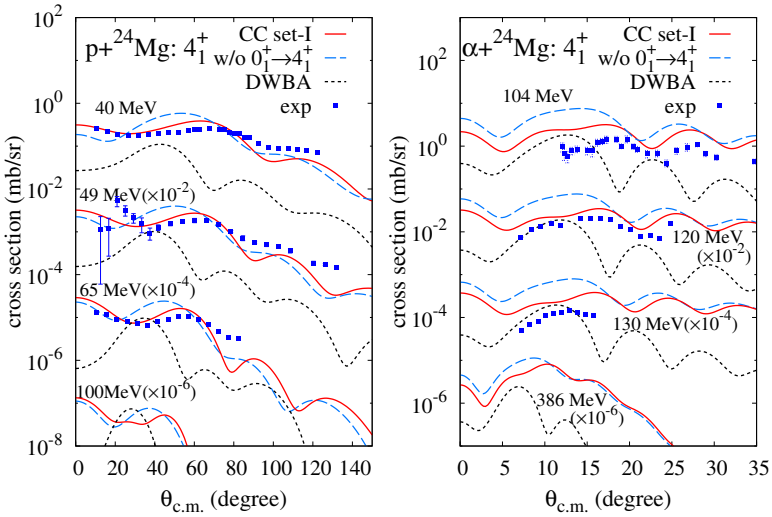

Fig. 7. The MCC+AMD results with and without the $0^+_1 \to 4^+_1$ transitions of the (p,p') and (α,α') cross sections to the 4^+_1 state of ^{24}Mg, obtained with the present AMD(fix-s) calculation using $f^{\rm tr}$(set-I). The full CC calculation including the $0^+_1 \to 4^+_1$ transitions (CC set-I) and the CC calculation without the $0^+_1 \to 4^+_1$ transition are shown by solid and dashed lines, respectively. The one-step (DWBA) cross sections (dotted lines) are also shown for comparison. The experimental (p,p') data are from Refs. [13,17,19,20,62], and the (α,α') data are from Refs. [31–33,62].

These data should be reexamined by the careful separation of the weak 4^+_1(4.12 MeV) spectra from the strong 2^+_2 spectra of the inelastic scatterings.

Figure 8 compares the present and previous results of MCC+AMD for the 4^+_1 cross sections obtained with the AMD(fix-s) and AMD(opt-s) densities, respectively. The present calculation employing the AMD(fix-s) densities successfully reproduces the angular distributions of the (p,p') and (α,α') cross sections, whereas inconsistent results were obtained in the previous calculation using the AMD(opt-s) densities because the $E4; 0^+_1 \to 4^+_1$ transition density of AMD(opt-s) was incorrect (refer to the charge form factors in Fig. 3(d)). In the results obtained with the AMD(opt-s) densities, the direct $0^+_1 \to 4^+_1$ transition gives a minor contribution to the 4^+_1 cross sections, and the full CC result is consistent with the CC calculation without the $0^+_1 \to 4^+_1$ transition. In other words, the success of the present MCC+AMD calculation is because of the detailed description of the $0^+_1 \to 4^+_1$ transition density, which is essential for the deconstructive interference of the strong two-step process by the weak one-step process in the 4^+_1 cross sections. This result indicates that the MCC approach is beneficial to examine the validity of the structure inputs even if the one-step contribution is not dominant. Notably, it is proved that the MCC approach combined with the microscopic structure calculation is necessary to solve the puzzle in the 4^+_1 cross sections.

In the detailed comparison of the preset result with the observed data, there is a slight overestimation of the (α,α') cross sections of the 4^+_1 state. To observe the effect of the ambiguity in the $E2; 4^+_1 \to 2^+_1$ transition strength to the 4^+_1 cross sections, we conduct the MCC+AMD calculation for $f^{\rm tr}$(set-II). Figure 8 shows a comparison of the results of $f^{\rm tr}$(set-I) and $f^{\rm tr}$(set-II). The difference between the set-I and -II calculations is only a slight modification in the renormalization factor of the $E2; 4^+_1 \to 2^+_1$ transition density; it changes from $f^{\rm tr}$(set-I) $= 1.26$ to $f^{\rm tr}$(set-II) $= 1.11$. Regarding set-II, $f^{\rm tr}$(set-II) of 1.11 for $4^+_1 \to 2^+_1$ coincides with $f^{\rm tr}$ of 1.12 for the $2^+_1 \to 0^+_1$ transition in the same band. By this modification, the 4^+_1 cross sections are slightly reduced, especially for the α scattering, and better

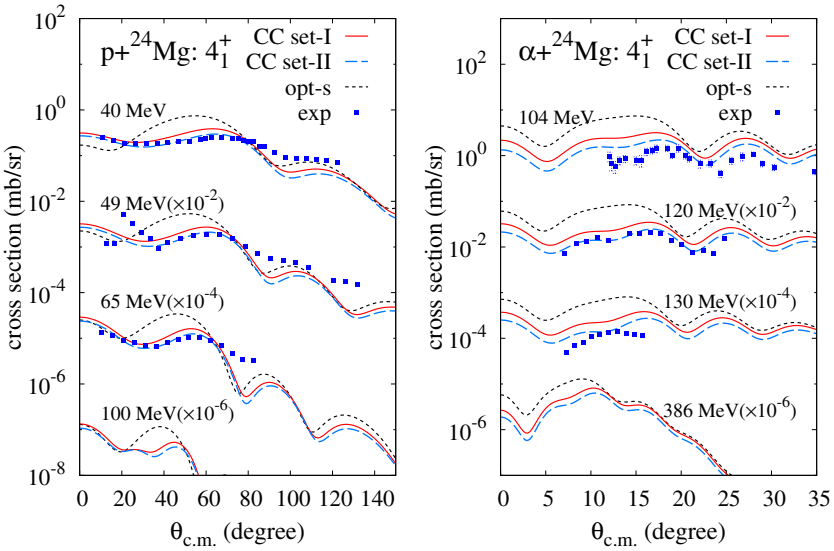

Fig. 8. Inelastic proton and α scattering cross sections of the 4^+_1 state of ^{24}Mg calculated by MCC+AMD employing the AMD(fix-s) densities in the two renormalization factor cases, $f^{\rm tr}$(set-I) and $f^{\rm tr}$(set-II). The previous MCC+AMD results employing the AMD(opt-s) densities [37] are also shown. The experimental (p,p') data are taken from Refs. [13,17,19,20,62], and the (α,α') data are from Refs. [31–33,62].

results are obtained in set-II than in set-I. This implies that the value $f^{\rm tr} = 1.11$ for the $E2; 4^+_1 \to 2^+_1$ transition, which is adjusted to $B(E2; 4^+_1 \to 2^+_1) = 125\, e^2{\rm fm}^4$, is favorable to describe the 4^+_1 cross sections in the present MCC+AMD approach, although we cannot propound a definite conclusion because of the possible ambiguities in other transitions.

5. Summary

The structure and transition properties of the $K^\pi = 0^+$ and $K^\pi = 2^+$ bands of ^{24}Mg were investigated by microscopic structure and reaction calculations via inelastic proton and α scattering. For the structure calculation, we adopted AMD+VAP with fixed nucleon spins, called AMD(fix-s), instead of the previous AMD+VAP calculation with optimized nucleon spins, which we called AMD(opt-s). Employing the revised structure calculation (AMD(fix-s)), the $E4$ transitions to the 4^+_1 and 4^+_2 states were reexamined.

Employing the AMD(fix-s) calculation of the ^{24}Mg structure, improved results for the energy of the $K^\pi = 2^+$ band and the $E2$ and $E4$ transition strengths, which the previous AMD(opt-s) calculation could not quantitatively reproduce, were obtained. These improvements were obtained because of the enhanced triaxiality achieved by the AMD(fix-s) calculation. For the transition properties of the 4^+ states, a significant improvement was obtained for the $E4$ charge form factors by the AMD(fix-s) result. The remarkable difference between the 4^+_1 and 4^+_2 states of the charge form factors, which was observed by electron scattering, was described well by the AMD(fix-s) calculation. in particular, the calculation successfully reproduced the unusual behavior of the 4^+_1 form factors with a narrow two-peak structure. This structure corresponded to the enhanced outer amplitude of $\rho^{\rm tr}$, which was different from the conventional shape of standard $E4$ transitions. This is the first microscopic calculation that described this unique property of the $E4; 0^+_1 \to 4^+_1$ transition.

Employing the renormalized AMD(fix-s) densities, the MCC calculations of the proton and α scattering off ^{24}Mg were performed utilizing the Melbourne g-matrix effective interaction. The

MCC+AMD calculation in this study reasonably reproduced the elastic and inelastic cross sections of proton scattering in the energy range $E_p = 40$–100 MeV. For the α scattering, the calculation reproduced the amplitudes and angular distributions of the existing data adequately at an energy range of $E_\alpha = 100$–400 MeV. In particular, the present calculation with the AMD(fix-s) densities was in good agreement with the (p,p') and (α,α') data for the 4^+_1 state, which has long been a challenge to explain via reaction calculations. In the detailed analysis of the CC calculations with and without the $0^+_1 \to 4^+_1$ transition and the DWBA calculation, it was revealed that the dominant two-step process via the $E2; 0^+_1 \to 2^+_1$ and $E2; 2^+_1 \to 4^+_1$ transitions and the deconstructive interference by the weak one-step process were essential for the inelastic proton and α scattering to the 4^+_1 state.

The present results indicated that the MCC approach was beneficial for examining the validity of the structure inputs even if the one-step contribution was not dominant. The MCC approach combined with the microscopic structure calculation, which afforded correct charge form factors, was necessary for solving the puzzle in the proton and α inelastic scattering to the 4^+_1 state of ^{24}Mg.

In the structure calculation, better results for the $K^\pi = 2^+$ side-band were obtained with the present AMD(fix-s) calculation. However, the present framework of the AMD(fix-s) is not suitable to describe $1p$–$1h$ excitations including negative-parity states because nucleon spin degrees of freedom are frozen in the model space. For further improvement of the structure calculation for various excited states of ^{24}Mg, an extension of the model space beyond a one-Slater-determinant description, for example, the generator coordinate method using parameters for β_2, γ, and β_4 deformations, is necessary.

Acknowledgements

The computational calculations of this work were performed using the supercomputer at the Yukawa Institute for Theoretical Physics at Kyoto University. The work was supported by Grants-in-Aid of the Japan Society for the Promotion of Science (Grant Nos. JP18K03617, JP16K05352, and 18H05407) and by a grant of the joint research project of the Research Center for Nuclear Physics at Osaka University.

References

[1] D. Branford, A. C. McGough, and I. F. Wright, Nucl. Phys. A **241**, 349 (1975).
[2] L. K. Fifield, E. F. Garman, M. J. Hurst, T. J. M. Symons, F. Watt, C. H. Zimmerman, and K. W. Allen, Nucl. Phys. A **322**, 1 (1979).
[3] J. Keinonen, P. Tikkanen, A. Kuronen, Á. Z. Kiss, E. Somorjai, and B. H. Wildenthal, Nucl. Phys. A **493**, 124 (1989).
[4] Y. Horikawa, Y. Torizuka, A. Nakada, S. Mitsunobu, Y. Kojima, and M. Kimura, Phys. Lett. B **36**, 9 (1971).
[5] Y. Horikawa, Prog. Theor. Phys. **47**, 867 (1072).
[6] A. Nakada and Y. Torizuka, J. Phys. Soc. Jpn **32**, 1 (1972).
[7] A. Johnston and T. E. Drake, J. Phys. A: Math. Nucl. Gen. **7**, 898 (1974).
[8] G. C. Li, M. R. Yearian, and I. Sick, Phys. Rev. C **9**, 1861 (1974).
[9] H. Zarek et al., Phys. Lett. B **80**, 26 (1978).
[10] H. Zarek, S. Yen, B. O. Pich, T. E. Drake, C. F. Williamson, S. Kowalski, and C. P. Sargent, Phys. Rev. C **29**, 1664 (1984).
[11] G. S. Blanpied et al., Phys. Rev. C **41**, 1625 (1990).
[12] G. Haouat, C. Lagrange, R. de Swiniarski, F. Dietrich, J. P. Delaroche, and Y. Patin, Phys. Rev. C **30**, 1795 (1984).
[13] B. Zwieglinski, G. M. Crawley, H. Nann, and J. A. Nolen Jr., Phys. Rev. C **17**, 872 (1978).
[14] B. Zwieglinski, G. M. Crawley, W. Chung, H. Nann, and J. A. Nolen Jr., Phys. Rev. C **18**, 1228 (1978).
[15] R. de Swiniarski, C. Glashausser, D. L. Hendrie, J. Sherman, A. D. Bacher, and E. A. McClatchie, Phys. Rev. Lett. **23**, 317 (1969).
[16] R. De Swiniarski, A. Genoux-Lubain, G. Bagieu, J. F. Cavaignac, D. H. Worledge, and J. Raynal, Phys. Lett. B **43**, 27 (1973).

[17] A. A. Rush, E. J. Burge, V. E. Lewis, D. A. Smith, and N. K. Ganguly, Nucl. Phys. A **104**, 340 (1967).
[18] A. A. Rush and N. K. Ganguly, Nucl. Phys. A **117**, 101 (1968).
[19] S. Kato et al., Phys. Rev. C **31**, 1616 (1985).
[20] Y. S. Horowitz, N. K. Sherman, and R. E. Bell, Nucl. Phys. A **134**, 577 (1969).
[21] J. Eenmaa, R. K. Cole, C. N. Waddell, H. S. Sandhu, and R. R. Dittman, Nucl. Phys. A **218**, 125 (1974).
[22] R. M. Lombard, J. L. Escudié, and M. Soyeur, Phys. Rev. C **18**, 42 (1978).
[23] L. Ray, G. S. Blanpied, and W. R. Coker, Phys. Rev. C **20**, 1236 (1979).
[24] G. Blanpied, N. M. Hintz, G. S. Kyle, J. W. Palm, R. Liljestrand, M. Barlett, C. Harvey, G. W. Hoffmann, L. Ray, and D. G. Madland, Phys. Rev. C **20**, 1490 (1979).
[25] R. De Leo, G. D'Erasmo, E. M. Fiore, A. Pantaleo, M. Pignanelli, and H. V. Geramb, Phys. Rev. C **20**, 13 (1979).
[26] R. De Leo, G. D'Erasmo, A. Pantaleo, M. N. Harakeh, S. Micheletti, and M. Pignanelli, Phys. Rev. C **23**, 1355 (1981).
[27] K. Amos and W. Bauhoff, Nucl. Phys. A **424**, 60 (1984).
[28] R. J. Griffiths, Nucl. Phys. A **102**, 329 (1967).
[29] K. Van Der Borg, M. N. Harakeh, and B. S. Nilsson, Nucl. Phys. A **325**, 31 (1979).
[30] I. M. Naqib and J. S. Blair, Phys. Rev. **165**, 1250 (1968).
[31] H. Rebel, G. W. Schweimer, G. Schatz, J. Specht, R. Löhken, G. Hauser, D. Habs, and H. Klewe-Nebenius, Nucl. Phys. A **182**, 145 (1972).
[32] K. Van Der Borg, M. N. Harakeh, and A. Van Der Woude, Nucl. Phys. A **365**, 243 (1981).
[33] S. Adachi et al., Phys. Rev. C **97**, 014601 (2018).
[34] K. Siwek-Wilczyńska, J. Wilczyński, and P. R. Christensen, Nucl. Phys. A **229**, 461 (1974).
[35] Y. K. Gupta et al., Phys. Lett. B **806**, 135473 (2020).
[36] H. Sagawa and B. A. Brown, Phys. Lett. B **150**, 247 (1985).
[37] Y. Kanada-En'yo and K. Ogata, Phys. Rev. C **103**, 024603 (2021) [arXiv:2010.07578 [nucl-th]] [Search INSPIRE].
[38] Y. Kanada-Enyo and H. Horiuchi, Prog. Theor. Phys. **93**, 115 (1995).
[39] Y. Kanada-En'yo, H. Horiuchi, and A. Ono, Phys. Rev. C **52**, 628 (1995).
[40] Y. Kanada-En'yo, Phys. Rev. Lett. **81**, 5291 (1998).
[41] Y. Kanada-En'yo, M. Kimura, and A. Ono, Prog. Theor. Exp. Phys. **2012**, 01A202 (2012).
[42] Y. Kanada-En'yo and K. Ogata, Phys. Rev. C **99**, 064601 (2019).
[43] Y. Kanada-En'yo and K. Ogata, Phys. Rev. C **99**, 064608 (2019).
[44] Y. Kanada-En'yo and K. Ogata, Phys. Rev. C **100**, 064616 (2019).
[45] Y. Kanada-En'yo and K. Ogata, Phys. Rev. C **101**, 064607 (2020).
[46] Y. Kanada-En'yo and K. Ogata, Phys. Rev. C **101**, 064308 (2020).
[47] K. Ogata, Y. Chiba, and Y. Sakuragi, arXiv:2001.09627 [nucl-th] [Search INSPIRE].
[48] K. Amos, P. J. Dortmans, H. V. von Geramb, S. Karataglidis, and J. Raynnal, in Advances in Nuclear Physics edited by J. W. Negele and E. Vogt (Springer US, 2000), pp. 276–536.
[49] R. Machleidt, K. Holinde, and Ch. Elster, Phys. Rep. **149**, 1 (1987).
[50] K. Minomo, K. Ogata, M. Kohno, Y. R. Shimizu, and M. Yahiro, J. Phys. G: Nucl. Part. Phys. **37**, 085011 (2010).
[51] M. Toyokawa, K. Minomo, and M. Yahiro, Phys. Rev. C **88**, 054602 (2013).
[52] K. Egashira, K. Minomo, M. Toyokawa, T. Matsumoto, and M. Yahiro, Phys. Rev. C **89**, 064611 (2014).
[53] K. Minomo and K. Ogata, Phys. Rev. C **93**, 051601(R) (2016).
[54] K. Minomo, K. Washiyama, and K. Ogata, arXiv:1712.10121 [nucl-th] [Search INSPIRE].
[55] Y. Kanada-En'yo, Phys. Rev. C **71**, 014303 (2005).
[56] Y. Kanada-En'yo, Phys. Rev. C **84**, 024317 (2011).
[57] T. Ando, K. Ikeda, and A. Tohsaki-Suzuki, Prog. Theor. Phys. **64**, 1608 (1980).
[58] R. Tamagaki, Prog. Theor. Phys. **39**, 91 (1968).
[59] N. Yamaguchi, T. Kasahara, S. Nagata, and Y. Akaishi, Prog. Theor. Phys. **62**, 1018 (1979).
[60] R. B. Firestone, Nucl. Data Sheets **108**, 2319 (2007).
[61] A. J. Koning and J. P. Delaroche, Nucl. Phys. A **713**, 231 (2003).
[62] N. Otuka et al., Nucl. Data Sheets **120**, 272 (2014).
[63] E. F. Hefter, Lett. Nuovo Cim. **24**, 425 (1979).